*Progress In Electromagnetics Research B, Vol. 99, 1–21, 2023*

# Simulation of Rapid Voltage Edge Related Voltage Surges in Highly Inductive Windings with Frequency Dependent Parameters

**Roberto Felicetti*, Jesus J. Perez-Loya, and Claes U. Lundin**

**Abstract**—Many static and rotating electric energy converters make use of inductive coils as filters, reactive loads or exciters, where a sudden variation of the magnetizing current can produce severe overvoltage with potential subsequent insulation damage. In some applications overvoltage is the result of a superposition of travelling voltage waves in a supplying line. Traditional tools for studying such phenomena are based on ordinary differential equations that can heavily handle variable parameters, especially if they change according to the rapidity of the observed overvoltage. In this paper the transient voltage distribution in the excitation winding of a salient pole synchronous generator is simulated by solving the problem entirely in the frequency domain, i.e., without any use of the traditional ordinary differential equations solvers. This makes it possible to tune the parameters of a simplified electric model to the frequency response of the studied winding. It is shown that for highly inductive windings a single transmission line model with frequency dependent parameters can reproduce voltage transients very accurately, in a broad interval of frequency, relevant for power electronics and electromagnetic compatibility applications. Furthermore, the paper presents the experimental setup which has been needed for generating the fast varying voltage edges.

## 1. INTRODUCTION

The energy stored in a magnetic field cannot be altered, transferred or converted instantaneously by means of electrical systems of finite power. This is why any attempt to change the instantaneous current sustaining a magnetic field is always delayed by the reaction of a self-induced Electromotive Force (EMF). This mechanism underlies many of the surge phenomena observed in the electrical systems. Switching overvoltages arise in power systems as soon as the current is disrupted or reinstated abruptly [1]. For highly inductive components, like transformers at no-load, shunt reactors and high voltage (HV) tertiary-windings for reactive power compensation [2–4], the voltage surge generated by the switching operations can be exceptionally high. In some cases, it can exceed even three times the nominal voltage. However, the relatively small inductance of a supply line (feeder) can produce a relevant voltage surge as well. The oscillation of energy, between the magnetic and electrostatic fields in the feeder-load system, produces a pseudo-periodic sequence of damped voltage overshoots at the termination of the supply line (ringing), which can be more than two times larger than the nominal voltage [5, 6]. The occurrence of these anomalous voltage levels in the power system poses a threat for the integrity of the insulating materials used in the electrical components. This is why the coordination of the insulation is an electrical engineering topic as old as the operation of the electrical power networks [7].

Moreover, the faster and faster commutation slew-rates, achieved thanks to the recent progresses in the Si- and SiC-switches technology [8, 9], are making the voltage surges relevant in low voltage (LV) applications as well [10–13]. The mechanism of the insulation failure at LV is more latent than

---

*Received 27 December 2022, Accepted 20 February 2023, Scheduled 6 March 2023*

* Corresponding author: Roberto Felicetti (roberto.felicetti@angstrom.uu.se).
The authors are with the Uppsala University, Sweden.

in the HV technology, since the insulation breakdown is less likely to happen at the time when the voltage surge takes place. Repeated overvoltage keeps degrading the insulation more and more through partial discharges (PD), each time that its level exceeds a so called inception voltage. In the end, the progressive wear and tear exerted by the PD establishes a breakdown path through the insulation, even though the applied electric field is way below the dielectric strength of the insulating material. Some recent studies [14, 15] have shown that the inception voltage does not depend on the type and geometry of the insulating material, or on the geometry of the electrodes (plates, rods, wires, bus-bars, etc.) only, but that the timing and shape of the voltage surge play a fundamental role too in triggering the PD mechanism. In particular, the amplitude of the voltage overshoots and the frequency of the ringing can make the PD more likely to happen.

The need for predicting the voltage surge in the windings of electrical machines driven by faster and faster switching power electronics devices has recently reignited the interest for consolidated simulation techniques, used for studying overvoltages in the power systems mainly. Bergeron's [16, 17] and Bewley's methods [18, 19], lumped-circuit [20], and single/multiple transmission line models (S/MTLM) [21] are among the most widely revived approaches. Nevertheless, these newly proposed simulation methods have to address the following requirements: a) the possibility to have an insight in different parts of the windings, cables, or lines for evaluating the overvoltages not just at their beginning and end; b) a higher level of accuracy in reproducing amplitude and timing of the overvoltage.

Bergeron's and Bewley's methods fail to accomplish point a) since they focus on the voltage propagation in the line only and represent the electrical machine at the line end by means of an equivalent concentrated impedance. Moreover, they cannot describe traveling waves in the windings themselves, since the voltage propagation in the electrical machines is transverse electromagnetic (TEM) at very slowly varying voltages only [22].

Lumped-circuits do not pose the same limitations as the previous models. Nevertheless, for rising fronts of the order of tenths of a nanosecond, the accuracy required in point b) can only be achieved by adopting a very small integration step and a very short discretizing length for the winding cell model. Both measures make the computational effort very heavy [24]. Besides, the timely solution of ordinary differential equations (ODE) with frequency dependent parameters requires special algorithms involving convolution integrals [25], which make the complexity of the problem even heavier.

The frequency dependency of the winding parameters is easier to be handled in the frequency domain, where it can be included in the transfer function of lump-circuited- or transmission-line-like-models [26, 27]. In that case, the cause of the surge under examination needs first to be Fourier-transformed. Then, the targeted effects in the frequency domain must be anti-transformed to the time domain in order to be observed and assessed. The capacity of this approach to fulfil requirement b) depends on both the accuracy of the model transfer function (TF) and the wideness of the frequency range where the TF is accurate [28]. The complexity of the problem at stake in this kind of model focuses on two main aspects: the number of poles and zeros to be included in the fit for the TF and the number of measurements to be performed in order to determine the parameters of the aforementioned fit [29]. However, some considerations presented in this paper, which apply very well to the windings wound on ferromagnetic cores, allow to simplify the model with frequency dependent parameters, with no need for a polynomial approximation of the voltage TF. A non-TEM Single Transmission Line Model (STLM) with four parameters, two of which dependent on frequency, is suggested in this paper. It proves to be able to reproduce voltage transients accurately in a highly inductive winding. Moreover, its parameters keep their physical significance, which is otherwise lost in the models based on the TF parameters fitting. Contrary to the Bergeron's and Bewley's models, which give an insight on the transient phenomena at the beginning and at the end of the winding only, the suggested model can describe the voltage transient at every position along the winding length.

The general simulation approach suggested in this work focuses on the modelling of the field winding of Salient Pole Synchronous Machines (SPSM). In fact, some recent innovative applications of the excitation current control [30] make use of fast switching power electronics on such a highly inductive circuit, traditionally designed for low voltage DC-supply.

In the first part of the paper (see Table 1 below), some theoretical considerations supporting the simplification introduced in the high frequency winding model are presented. They are subsequently applied to the characterization of the frequency dependent parameters of the STLM representing the

**Table 1.** A highlight on the structure of the paper.

| | Activities | Goals |
|---|---|---|
| First part | Characterization of the STLM for the winding | To find out which parameters play a major role in the winding during fast transients |
| | Characterization of the STLM for the feeder | To find out which parameters play a major role in the cable during fast transients |
| Second part | First experiment (transient).<br>A fast rising edge voltage is applied to the winding terminals directly | Checking if the model can reproduce the winding subcritical behaviour (travelling voltage waves frequency depends on the winding parameters only) |
| | Second experiment (transient).<br>A fast rising edge voltage is applied to the winding terminals through a feeder | Checking if the model can reproduce the winding supercritical behaviour (winding voltages frequency depends on the feeder parameters essentially) |
| | Third experiment (periodic steady state).<br>A periodic triangular voltage with very slow rising time is applied to the winding terminals | Checking if the model works even at relatively low frequency, given its development, which has been focused mainly on fast voltage transients |

field winding in the frequency domain. Finally, the model is used for simulating the transient voltage propagation produced by a fast rising voltage front applied to the winding terminals, directly or through a feeder. At the end, the model is tested also at low frequency by studying its response to a triangular voltage source in periodic steady state. All achieved simulation results are compared with the experimental evidences and assessed.

## 2. METHOD

### 2.1. The Test Setup

The simulation of the transients in the time domain consists in reproducing the voltage responses of the field winding of a four pole 60 kVA SPSM to fast varying voltage fronts produced by the setup represented in Figure 1.

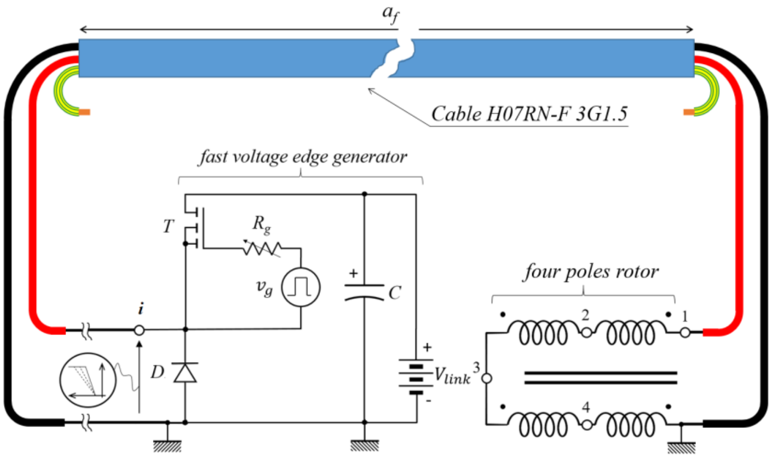

**Figure 1.** The application of fast rising voltage edges to the field winding of a SPSM.

An elementary generator of fast rising voltage edges with variable rise time is applied to the field winding of the test rotor (Figure 2) by means of an $a_f = 19.1\,\mathrm{m}$ long bipolar cable (feeder). Considering the field winding initially de-excited, when the enhancement N-channel MOSFET $T$ (FCH041N60F) is switched on, the DC-voltage $V_{link}$ is almost entirely transferred to the field winding. By adjusting the value of the gate resistance $R_g$ by means of a $1\,\mathrm{k\Omega}$ linear potentiometer, the rise time of the applied voltage can be varied continuously between 100 ns and 10 µs. In this way, the cascade of the feeder and the field winding can be supplied with step voltages showing different rise times.

**Figure 2.** The test field winding of a four solid pole salient pole rotor.

Moreover, the feeder can be removed so that the fast voltage edge generator directly supplies the field winding.

When rise times shorter than 100 ns are required for the test, the step voltage is generated by directly applying a DC voltage source to the field winding by means of a mechanical switch. Since the field winding is a highly inductive load, a flyback-diode 1N4003 is provided in parallel to it. This allows the field current to keep circulating in the winding for a longer time than the switch-off time of the MOSFET, preventing the insurgence of exceptionally large electromotive forces, potentially harmful for both the MOSFET and winding insulation.

In Figure 1, five different points ($i$, 1, 2, 3, 4) are shown, where the voltage responses to a given edge voltage can be measured towards ground. These represent the beginning of the feeding cable (point $i$) and the four taps of the winding (from 1 to 4), respectively. When the feeder is removed and the fast edge generator applied directly to the field winding, only four winding taps are available for the voltage detection. Finally, during the test in periodic steady state (triangular wave voltage), the field winding is directly supplied by using a function generator GwInstek SFG-1013 presenting $50\,\Omega$ internal resistance.

All measurements performed in the present work have been done with the rotor outside the stator bore and the field winding galvanically connected to the test setup (Figure 2). In fact, the relatively low impedance of the carbon brushes together with the predominant damping effect of the eddy currents make the influence of the carbon brushes on the transient phenomena irrelevant.

### 2.2. Single Transmission Line Model of the Field Winding

The excitation winding of electrically excited salient pole synchronous machines consists of an even number of coils, usually series connected. All coils are wound on rotor poles. Coils are made of the same materials, so to confer uniform electric and magnetic properties to the entire winding. For that reason, an STLM with uniform parameters is suitable to reproduce the described electrical and magnetic uniformity of the rotor winding. Figure 3 shows the modelling of a differential linear part $dx$ of the field winding, taken at the generic distance $x$ along the wire, starting from the supplying voltage terminals [22].

The specific capacitance of the winding towards the grounded machine frame is taken into account by the capacitance per unit length $c$. This parameter is not affected by the presence of the machine armature and/or by the relative angular position between the rotor and stator due to the essentially complete electrostatic induction existing between the field winding and rotor frame [34]. The parameter $k$ considers the specific capacitive coupling between two adjacent turns of the winding. All magnetic influences, responsible for inducing an electromotive force (EMF) into the winding, are summarized by the inductance per unit length $l_w$. Finally, all non-conservative phenomena occurring in the winding are reproduced in the model through three distinct parameters: the specific winding AC-resistance $r_w$, considering the wire Joule losses in the presence of skin and proximity effect, the magnetic losses related specific parallel resistance $r_p$, and the dielectric losses related specific conductance $g$.

In the present work the effects of fast varying voltage fronts on highly inductive windings are primarily addressed, so that the circuit of Figure 3 is interested by high frequency components of the voltage. In Figure 4, three different voltage signals are represented, which share the same maximal value $V$ and rise time $\tau$: a step function (a), a single pulse with duration $T + 2\tau$ (b), and a triangular pulse with duration $2\tau$ (c).

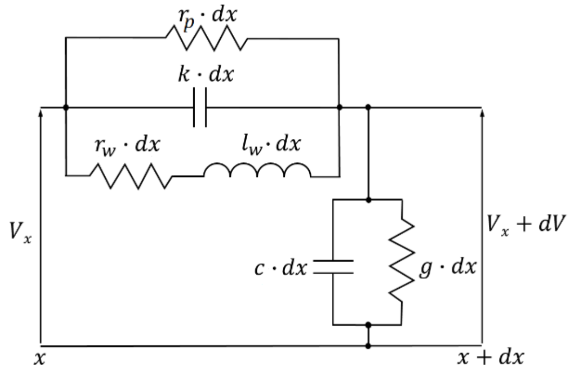

**Figure 3.** A differential linear part of the field winding according to the STLM [22].

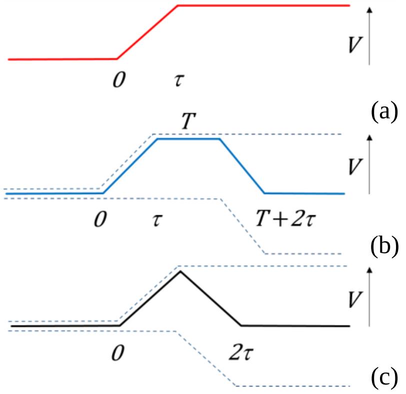

**Figure 4.** Different voltage signals: (a) step voltage, (b) single pulse, (c) triangular pulse.

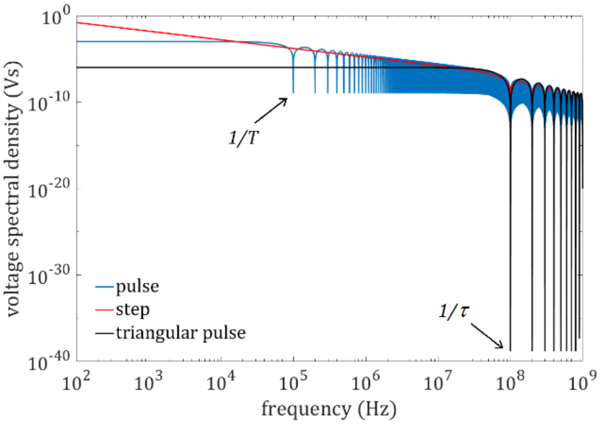

**Figure 5.** Spectral density of the voltage signals shown in Figure 4 for $V = 100\,\mathrm{V}$, $\tau = 10\,\mathrm{ns}$ and $T = 10\,\mu\mathrm{s}$.

Figure 5 helps to understand what the three signals have in common in the frequency domain. It shows the spectra of the three previous signals where, for the sake of clarity, arbitrary but plausible values of voltage and rise time for a common Si-MOSFET application have been chosen: $V = 100\,\mathrm{V}$, $\tau = 10\,\mathrm{ns}$, and $T = 10\,\mu\mathrm{s}$. It can be observed that the plots share their spectral lines starting from the frequency $1/\tau$. That points to the fact that the shared spectral content of the signals beyond the frequency $1/\tau$ is somehow related to their common rise time $\tau$.

Therefore, in order to study the behaviour of the winding towards rapid voltage edges, it is necessary to consider how the circuit of Figure 3 behaves primarily in the presence of high frequency voltages.

To that end, the first consideration is about the possibility of assuming the model as linear at high frequency, given that the winding is wound on a nonlinear ferromagnetic core. In this case, the low-pass filter effect of the winding, together with its large time constant (usually in the order of units or tenths of second in salient pole rotor excitation windings), provides a strong attenuation on the high frequency components of the excitation current. In other words, an AC-voltage having the amplitude comparable with the field winding rated DC-voltage does not manage to force an amplitude-like nominal current intensity into the excitation winding, once the winding cut-off frequency is exceeded. Moreover, the demagnetizing reaction of the eddy currents induced in the magnetic iron path opposes to the establishment of a main flux into the core, diverting it towards the intrapolar spaces as stray flux. These combined effects set the contributions of the high frequency voltage components to the magnetic flux in the rotor way below the nominal one. Therefore, the magnetic flux produced by fast voltage transients is far away from the upper knee of the machine magnetization curve and from the nonlinearity. Moreover, the eddy currents prevent the mutual magnetic coupling between windings turns which are not adjacent [31]. This makes it possible to consider the specific winding inductance $l_w$ as well as a specific self-inductance essentially.

A second consideration is about the role and relevance of the dissipative components in the circuit of Figure 3. The average energy, provided to the winding over one period by an AC supplying voltage, must be either dissipated in heat (in the wire, in the iron, in the insulating material), or it must leave the winding as a radio wave. In the last case, the wave length of the voltage perturbation propagating into the winding must be comparable with the wire length in order to make an antenna of it. However, observing the circuit of Figure 1, it is possible to recognize a parallel resonant structure formed by the specific inductance $l_w$ and specific elastance $k$. For supercritical frequencies, which exceed the critical frequency of the winding

$$f_c = \frac{1}{2\pi}\sqrt{\frac{k}{l_w}}, \tag{1}$$

the specific longitudinal impedance of the line

$$\bar{z} = \left(\frac{1}{r_w + j\omega l_w} + \frac{j\omega}{k} + \frac{1}{r_p}\right)^{-1} \tag{2}$$

would become predominantly capacitive and confer a capacitive nature to the input impedance of the winding. Since the supercritical voltage waves led by a feeding cable and hitting the winding evolve quicker than the time needed for the propagation to go forth and back through the winding itself, they experience the characteristic impedance of the winding at the winding terminals. Since the characteristic impedance of the winding is usually way larger than that of the feeder, a harmonic voltage wave, travelling through a cable towards the rotor winding and showing a frequency higher than $f_c$, undergoes a voltage reflection at the windings terminals. It manages to partially energize the electrostatic mode of the winding at the cost of a voltage drop of the incident wave and gets reflected back as a regressive voltage wave. Moreover, the phenomenon of the modal dispersion [22] shows that beyond the critical frequency there is no wave propagation based on conduction current into the winding. All these considerations let us conclude that the radiative power from the winding must be negligible in comparison with the other kind of losses and that the parameter $g$ in the model eventually takes into account the dispersion and relaxation losses of the winding insulation only. The specific winding conductance $g$ is related to the specific ground capacitance $c$ through the loss factor

$$\tan\delta = \frac{g}{\omega c}. \tag{3}$$

The loss factor accounts for units or fraction of unit of percentage in the kHz frequency range, so that $g$ can be neglected in a simplified version of the model of Figure 1.

The dissipative parameters $r_w$ and $r_p$ can also be compared with the specific winding reactance, since all of them are involved in determining the specific longitudinal impedance of the winding. Considering the expulsion of the flux from the ferromagnetic circuit operated by the eddy currents, the linked flux of the winding at high frequency mainly crosses the air and the copper of the pole coils. Nevertheless, the skin and proximity effects manage to segregate the magnetic energy only in air essentially, as soon as the current in the copper is confined in a peripheral thin layer of the wire, as thick as the penetration depth

$$\delta_{Cu} = \sqrt{\frac{\rho_{Cu}}{\omega \mu_0}}. \tag{4}$$

The sketch of Figure 6 shows a unitary length of a twin-lead line with copper conductors, representing a portion of two neighbour turns of the winding. It establishes a magnetic field in air and partially in the round wires, under the effect of a high frequency current $\bar{I}$(A).

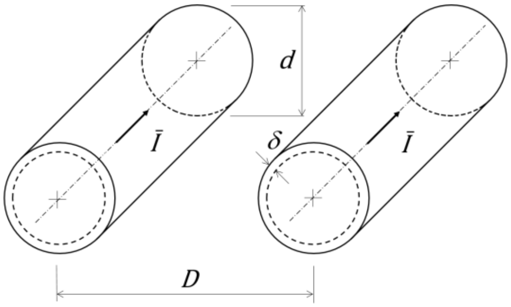

**Figure 6.** Geometry of a unitary double-lead line at high frequency.

Considering the geometry of the line presented in Figure 6 [23] and Equation (4), it is possible to express the ratio between the specific reactance and resistance of the wire as

$$\frac{\omega l_w}{r_w} \cong \frac{\omega \mu_0}{\pi} \left[ \ln \left( \frac{2l}{\sqrt{dD}} \right) \right] \cdot \frac{\pi d \delta_{Cu}}{\rho_{Cu}} \propto \frac{d}{\delta_{Cu}}, \tag{5}$$

having neglected the small magnetic energy internal to the copper.

It can be recognized through (4) and (5) that, when the frequency increases, the wire reactance $\omega l_w$ ($\Omega$ m$^{-1}$) prevails over the wire resistance $r_w$. If the capture of the main flux through the eddy currents (degaussing) should not be as effective as hypostatised above, the resulting lower reluctance of the ferromagnetic circuit would make the specific reactance of the winding even larger than imagined. Moreover, leaving aside the specific DC design of the excitation winding considered here, all technical expedients used in the AC windings for limiting the skin and proximity effects magnify the relative weight of the specific winding reactance to the specific winding resistance in (5). For all the reasons given, in the simplified high frequency model for the circuit of Figure 3, the conduction current through the winding is essentially limited by the sole action of the specific inductance.

Coming to the specific parallel resistance $r_p$, the sketch in Figure 7 shows the eddy current density $\bar{J}$ (A m$^{-2}$) induced in a thin ferromagnetic sheet of the rotor magnetic circuit by the harmonic flux density $\bar{B}$ (T).

This current can be regarded as the secondary current of a transformer, the primary of which is formed by the series of $2p$ pole windings of $N$ turns each. The ratio between the specific reactance of the winding and the secondary specific resistance referred to the primary is then

$$\frac{\omega l_w}{r_p} \cong \omega p \left(2N\right)^2 \mu_{Fe} b w \cdot \left(\frac{1}{2N}\right)^2 \frac{\delta_{Fe}}{2p \rho_{Fe} b} \propto \frac{w}{\delta_{Fe}}, \tag{6}$$

where

$$\delta_{Fe} = \sqrt{\frac{\rho_{Fe}}{\omega \mu_{Fe}}} \tag{7}$$

is the penetration depth of the eddy current density in the ferromagnetic laminate for the angular frequency $\omega$ (rad s$^{-1}$).

Observing (6) and (7), it can be recognized that the specific wire reactance $\omega l_w$ prevails on the parallel wire resistance $r_p$ for increasing frequency. Since $r_p$ is in parallel with the specific reactance, the resistance cannot be neglected at high frequency and must be considered in the simplified version of the circuit of Figure 3.

In considering the specific parameters which are responsible for the damping of the pseudo-periodic voltage overshoots in the transformer winding, Heller and Veverka [32] have found the following expression for the voltage decay rate $\gamma$ ($s^{-1}$)

$$\gamma = -\frac{r_w}{2l_w} - \frac{l_w}{2r_p}\omega^2. \tag{8}$$

Equation (8) shows that for

$$f < f^* = \frac{\sqrt{r_w r_p}}{2\pi l_w} \tag{9}$$

the winding Joule losses set the attenuation mechanism for the overvoltages. At higher frequency, for $f > f^*$, the iron losses dominate instead. Since the second term in the right side of (8) grows faster in frequency than the first one, the transition frequency $f^*$ does not exceed a few hundreds of Hz. The predominant role of $r_p$, rather than $r_w$ in reproducing the attenuation for the travelling waves in the kHz range, supports in the end the neglecting of $r_w$ from the circuit of Figure 3. Figure 8 represents the final 4-parameters model used in this work for simulating the fast voltage transients in the field winding of a salient pole synchronous machine.

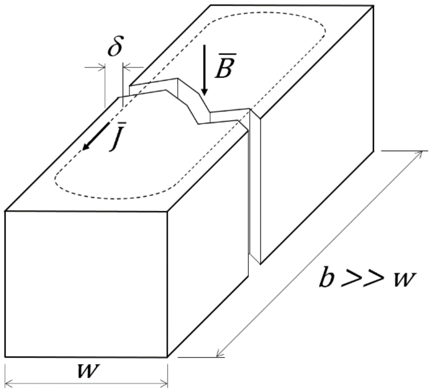

**Figure 7.** Eddy current density in a thin ferromagnetic laminate of the winding core.

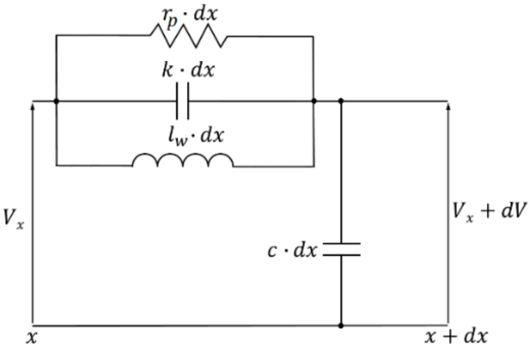

**Figure 8.** Simplified STLM of the field winding for fast voltage transient simulation.

## 2.3. Single Transmission Line Model of the Feeder

The line connected to the rotor winding (feeder) consists normally either of bipolar bus-bars or a two-wire cable which connect the cabinet of the Excitation System (ES) to the excitation winding. The more or less long feeder conductors present a cross sectional area similar to that of the winding wire. In the present work, a double-lead feeder with ethylene propylene rubber (EPR) insulation has been used, since it was available in the laboratory. It is made of the phase and neutral conductors of a three-polar H07RN-F cable with protective earth wire (PE). Figure 9 shows the cross section of the feeder with its main geometric dimensions.

The feeder presents homogeneous electrical properties along its length $a_f$ (m), which can be well represented by a TEM-STLM with uniformly distributed parameters. Figure 10 shows the electric model for an infinitesimal length $dx$ of the cable of Figure 9.

The specific external inductance of the feeder can be found by

$$l_{f,ext} = \frac{\mu_0}{\pi}\cosh^{-1}\frac{D_i}{D_w}, \tag{10}$$

whereas the internal inductance for DC current is equal to

$$l_{f,int}\left(DC\right) = \frac{\mu_0}{4\pi}. \tag{11}$$

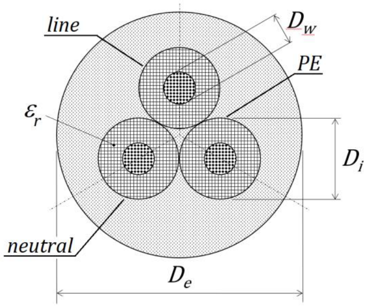

**Figure 9.** Feeder cross section with main dimensions.

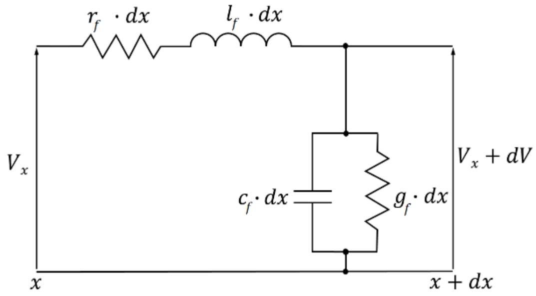

**Figure 10.** STLM of the feeder.

When the current density concentrates close to the outer surface of solid conductors, the contribution of the internal inductance to the total conductor inductance fades away. In this case, since the cable has stranded conductors, where the strands are twisted or transposed, the current in the conductor cross-section remains almost uniform when the frequency increases.

The specific capacitance $c_2$ between two conductors of the cable, once the third one has been removed, is

$$c_2 = \frac{\pi\varepsilon_r\varepsilon_0}{\cosh^{-1}\frac{D_i}{D_w}}. \tag{12}$$

The presence of the third conductor PE induces more charge on the line and on the neutral conductor making the specific capacitance of the two-wire cable one and half times larger than $c_2$

$$c_f = {}^3\!/_2\, c_2 = {}^3\!/_2 \frac{\pi\varepsilon_r\varepsilon_0}{\cosh^{-1}\frac{D_i}{D_w}}. \tag{13}$$

The specific DC resistance of the cable depends on the resistivity of the copper $\rho_{Cu}$, on the number of strands $n_s$ in the conductor, and on the strand diameter $D_s$

$$r_{f,DC} = 4\xi\frac{\rho_{Cu}}{n_s D_s^2}, \tag{14}$$

where the parameter $\xi(-)$ takes into account the relative increase of the wire length due the twisting or the transposition of the strands in the bundle.

The specific AC-resistance $r_f$ increases with the frequency due to the skin-effect and the proximity-effect in the wire strands. The expressions for $r_f$ change if the strand cross section is fully penetrated by the current or not. In the Appendix to the present work, some formulas have been derived for estimating the frequencies which discriminate between the full and partial penetrations of the feeder conductors.

With reference to the skin effect, the frequency beyond which the strand can be considered not fully penetrated can be estimated by (see (A20) in Appendix A)

$$f_{skin\_pp} = \frac{8}{\pi}\frac{\rho}{\mu_0 D_s^2}. \tag{15}$$

With reference to the proximity effect instead, the frequency which discriminates between the two conditions of penetration gives (see (A15) in Appendix A)

$$f_{dis} = \frac{8\sqrt[3]{2}}{\pi}\frac{\rho}{\mu_0 D_s^2}. \tag{16}$$

For an AWG16 cable with stranded conductors, where $n_s = 27$, $D_s = 0.26\,\text{mm}$, $D_w = 1.3\,\text{mm}$, from (15) and (16) the reference frequencies $f_{skin\_pp} = 539.6\,\text{kHz}$ and $f_{dis} = 679.8\,\text{kHz}$ are obtained. Assuming a relative permittivity $\varepsilon_r = 3$ for the rubber insulation in the cable and the distance $D_i = 3.3\,\text{mm}$ between the axes of the phase conductors, from (10), (11), and (13) the reference values $l_f = 0.73\,\mu\mathrm{Hm}^{-1}$ for the specific feeder inductance and $c_f = 79.1\,\mathrm{pFm}^{-1}$ for the specific feeder capacitance can be found. The expected frequency of the ringing per meter feeder can be roughly estimated considering a fourth of wave resonance in this cable, with the terminals short-circuited at the beginning and open at the end

$$f_{\lambda/4} = \frac{1}{4\sqrt{l_f c_f}} = 33\,\mathrm{MHzm}. \tag{17}$$

From Equation (17), it can be concluded that for a feeder length shorter than 40 m the frequency of the ringing is such to require a partially penetrated model in order to take into account the skin effect and the proximity effect in the specific cable resistance. In the Appendix the following model for the feeder AC-resistance has been obtained

$$r_f = r_{f,DC}\left(F_{skin} + F_{prox}\right) \tag{18}$$

where

$$F_{skin} = \frac{D_s}{4\delta} + \frac{1}{4} + \frac{3}{16}\frac{\delta}{D_s} \tag{19}$$

and

$$F_{prox} = \frac{1}{64\sqrt{2}\pi^2}\frac{D_s}{\delta}\left(\frac{n_s D_s}{D_w}\right)^2. \tag{20}$$

The specific conductance $g_f$ can be hardly calculated. As a reference, cross-linked polyethylene (XLPE) cables with zero hours of service show loss factor in the order of $10^{-2}$ in the MHz range. If semi-conductive layers coat the conductors, the same parameter can reach and exceed $10^{-1}$ [33]. The EPR insulation of the feeder used in the test setup has a higher relative permittivity than XLPE knowingly. This causes higher relaxation losses. Moreover, the presence of the floating PE conductor in the H07RN-F cable of Figure 1 could generate additional losses, similar to those observed in the semiconducting layers of XLPE cables. It is anticipated here (see paragraph 3.2) that the found value for the cable loss angle amounts to $\delta_f \cong \tan\delta_f = 0.02$.

## 2.4. Transients and Periodic Steady State Simulations

The STLM of Figure 8 can be conveniently represented in the frequency domain by the system of complex equations

$$\begin{cases} \bar{V}_i = \cosh\bar{K}x \cdot \bar{V}_x + \bar{Z}_0 \sinh\bar{K}x \cdot \bar{I}_x \\ \bar{I}_i = {}^1\!/\!_{\bar{Z}_0} \sinh\bar{K}x \cdot \bar{V}_x + \cosh\bar{K}x \cdot \bar{I}_x \end{cases} \tag{21}$$

where

$$\bar{K} = \sqrt{\bar{z}\bar{y}} \tag{22}$$

is the propagation constant, and

$$\bar{Z}_0 = \sqrt{\bar{z}/\bar{y}} \tag{23}$$

is the characteristic impedance of the line.

For the $i$-th pole winding with wire length $a/4$, the Equation (21) becomes

$$\begin{bmatrix} \bar{V}_i \\ \bar{I}_i \end{bmatrix} = \begin{bmatrix} \bar{A} & \bar{B} \\ \bar{C} & \bar{D} \end{bmatrix} \begin{bmatrix} \bar{V}_{i+1} \\ \bar{I}_{i+1} \end{bmatrix} \tag{24}$$

where

$$\bar{A} = \bar{D} = \cosh\bar{K}\,{}^a\!/\!_4 \tag{25}$$

$$\bar{B} = \bar{Z}_0 \sinh\bar{K}\,{}^a\!/\!_4 \tag{26}$$

$$\bar{C} = {}^1\!/\!_{\bar{Z}_0} \sinh\bar{K}\,{}^a\!/\!_4. \tag{27}$$

The same formula (24) holds for the second, third, and forth pole windings, so that the entire rotor winding can be represented by the two-port networks cascade of Figure 11.

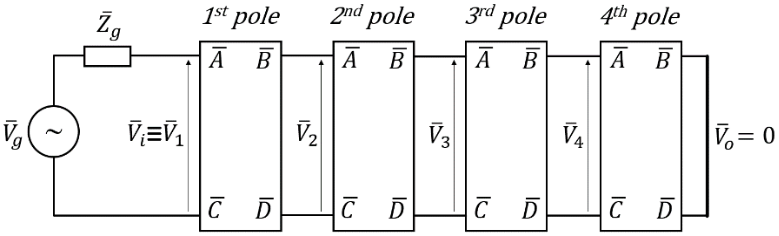

**Figure 11.** Two-port networks cascade representing the field winding.

Since the exit terminal of the last pole winding is grounded, the cascade is closed on a short-circuit, which forces the output voltage to zero.

The feeder model of Figure 10, showing the total length $a_f$, can be represented by (24) as soon as the following constants are used

$$\begin{aligned} \bar{A}_f &= \bar{D}_f = \cosh \bar{K}_f a_f && (28)\\ \bar{B}_f &= \bar{Z}_{0f} \sinh \bar{K}_f a_f && (29)\\ \bar{C}_f &= {}^{1}\!/\!_{\bar{Z}_{0f}} \sinh \bar{K}_f a_f, && (30) \end{aligned}$$

where $\bar{K}_f$ and $\bar{Z}_{0f}$ are the propagation constant and characteristic impedance of the feeder, respectively. The connection between the feeder and the field winding can be then obtained by adding the feeder related two-port network at the beginning of the two-port networks cascade of Figure 11, as shown in Figure 12.

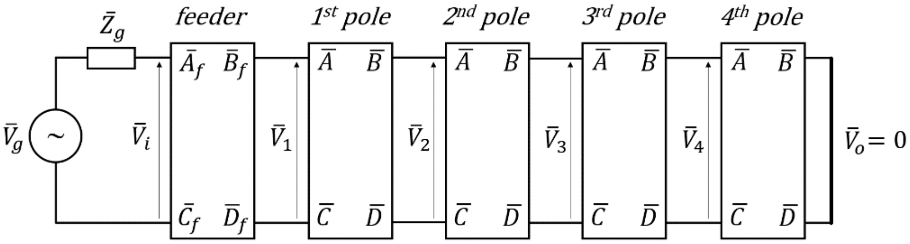

**Figure 12.** Two-port network cascade representing the feeder-field winding connection.

With reference to Figure 11, knowing the voltage $\bar{V}_i$ at the input of the two-port networks cascade, it is possible to find out the voltage $\bar{V}_n$ at the generic $n$-th interconnection between two poles (with $n = 1, 2, 3, 4$) by using the voltage transfer function $\bar{F}_n(j\omega)$

$$\bar{V}_n = \bar{F}_n(j\omega)\bar{V}_i, \tag{31}$$

where

$$\bar{F}_n(j\omega) = \left(\bar{A}_n + {}^{\bar{B}_n}\!/\!_{\bar{Z}_{in,n}}\right)^{-1}. \tag{32}$$

In Equation (32), $\bar{A}_n$ and $\bar{B}_n$ represent the open circuit reverse voltage transfer ratio and the short circuit reverse transfer impedance respectively for the $n-1$ two-port networks chain preceding the $n$-th pole windings interconnection. The quantity $\bar{Z}_{in,n}$ represents the input impedance of a cascade of $5-n$ two-port networks, which is short circuited at the output.

With reference to Figure 12, knowing the voltage $\bar{V}_i$ at the input of the two-port networks cascade, it is possible to find out the voltage $\bar{V}_n$ at the generic $n$-th interconnection between two pole windings (with $n = 1, 2, 3, 4$) by using the voltage transfer function $\bar{F}_{f,n}(j\omega)$

$$\bar{V}_n = \bar{F}_{f,n}(j\omega)\,\bar{V}_i, \tag{33}$$

where

$$\bar{F}_n\left(j\omega\right) = \left(\bar{A}_{f,n} + {}^{\bar{B}_{f,n}}\!/_{\bar{Z}_{in,n}}\right)^{-1}. \tag{34}$$

In Equation (34), $\bar{A}_{f,n}$ and $\bar{B}_{f,n}$ represent the open circuit reverse voltage transfer ratio and the short circuit reverse transfer impedance respectively, for the $n$ two-port networks chain preceding the $n$-th pole windings interconnection, including the one related to the feeder.

Figure 13 shows the procedure followed for simulating the first two tests by using the frequency dependent models of the field winding and, where present, of the feeder. After having taken $N$ samples of the input voltage $v_i$ at the interval of time $\Delta t_i$, the input signal is Fourier-transformed through a FFT routine. The latter gives $N$ values of the voltage spectral density at a distance of $\Delta f$ from each other. Each spectral density sample has its own frequency and can be processed in the frequency domain through the TF (32) or (34) in order to find the correspondent output voltage at a given position $x_j$ along the feeder-winding cascade of Figure 11 or Figure 12, respectively.

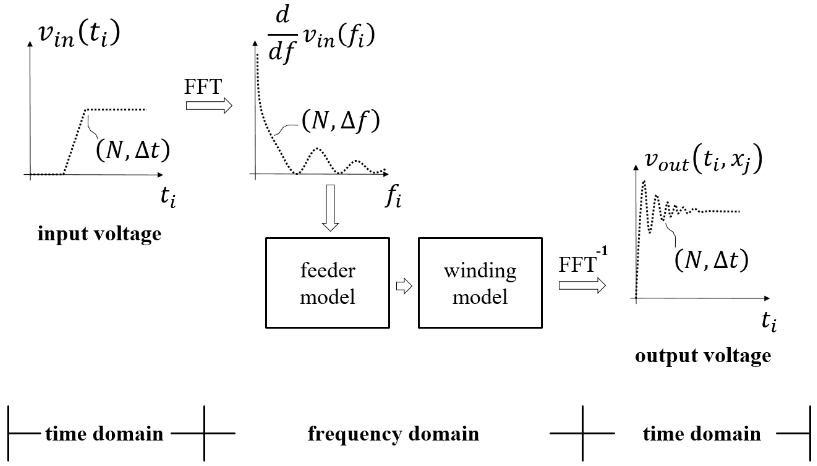

**Figure 13.** Flow-chart of the method followed for simulating test 1 and test 2.

If the input voltage $v_i(t)$ has a known Fourier transform

$$\tilde{V}_i\left(j\omega\right) = \Im\left[v_i\left(t\right)\right] \tag{35}$$

the response voltage $v_n(t)$ at the $n$-th interconnection between pole windings can be achieved straightforwardly by anti-transforming the frequency response of $\bar{F}_{f,n}(j\omega)$ to (35)

$$v_n\left(t\right) = \Im^{-1}\left[\tilde{V}_n\left(j\omega\right)\right] = \Im^{-1}\left[\bar{F}_{f,n}\left(j\omega\right)\tilde{V}_i\left(j\omega\right)\right]. \tag{36}$$

For a step function with amplitude $V$ and finite rise time $\tau$, like the one shown in Figure 2(a), the Fourier transform to be used in (36) is

$$\tilde{V}_i\left(j\omega\right) = V\tau\left(\frac{\sin{}^{\omega\tau}\!/_2}{{}^{\omega\tau}\!/_2}\right)^2\frac{e^{j\omega\tau}}{1-e^{j\omega\tau}}. \tag{37}$$

If the input voltage $v_i\left(t\right)$ is a periodic one instead, as it is the case in the third test, so that

$$v_i\left(t\right) = \sum_{k=1}^{\infty} b_k \sin\left[k\Omega t + \varphi_k\right], \tag{38}$$

the periodic steady state voltage response $v_n(t)$ to the input voltage (38) is given by

$$v_n\left(t\right) = \sum_{k=1}^{\infty} b_k\left|\bar{F}_{f,n}\left(j\Omega_k\right)\right|\sin\left[k\Omega t + \varphi_k + \angle\bar{F}_{f,n}\left(j\Omega_k\right)\right]. \tag{39}$$

## 3. RESULTS AND DISCUSSION

The electric parameters for the field winding of a 60 kVA SPSM have been measured according to [34], and their values are reported in Table 2.

**Table 2.** Distributed parameters of the field winding.

| $c$ | $k$ | $l_w$ | | $r_p$ | |
|---|---|---|---|---|---|
| | | $k_w$ | $\gamma_w$ | $k_p$ | $\gamma_p$ |
| [pFm$^{-1}$] | [μF$^{-1}$m$^{-1}$] | [mHm$^{-1}$] | [−] | [mΩm$^{-1}$] | [−] |
| 1.76 | 13.6 | 2.01 | −0.347 | 17.99 | 0.710 |

The dependency of the specific field winding inductance and resistance on the frequency is expressed [34] by

$$l_w = k_w f^{\gamma_w} \tag{40}$$

and

$$r_p = k_p f^{\gamma_p} \tag{41}$$

respectively.

The electric parameters of the $a_f = 19.1\,\mathrm{m}$ long feeder made of a H07RN-F 3G 1.5 mm$^2$ cable have been measured by means of the Q-meter (GenRad 1658 RLC Digibridge) at 1 kHz. For measuring the inductance and resistance, the cable has been short-circuited, whereas for measuring the capacitance it has been kept open at its end. The values determined by those ways are presented in Table 3.

**Table 3.** Electromagnetic parameters of the feeder (measured).

| $c_f$ | $l_f$ | $r_f$ |
|---|---|---|
| [pFm$^{-1}$] | [μFm$^{-1}$] | [mΩ] |
| 95.2 | 0.67 | 26.3 |

### 3.1. First Experiment and Subcritical Transient Simulation

The first experiment makes reference to the setup of the voltage propagation through the excitation winding. A 13 V large voltage step with rise time 0.2 μs is applied to the field winding terminals directly. The voltage responses have been detected by means of an oscilloscope at the interconnections between the pole windings. Following the order of the voltages presented in Figure 11, Figure 14 represents the comparison between the measured and simulated voltages.

In Figure 14, the frequency of the ringing in all three plots is almost 44 kHz, which corresponds to the first resonance frequency of the field winding. Substituting Equation (40) in the equation for the first natural frequency $f_1$ of the field winding given in [34] and solving for it, it is possible to obtain

$$f_1 = \left\{ 4\pi^2 k_w \left[ c\left(\frac{a}{\pi}\right)^2 + \frac{1}{k} \right] \right\}^{-\frac{1}{2+\gamma_w}} = 44.4\,\mathrm{kHz}. \tag{42}$$

It must be noticed how precisely the simulation fits to the amplitude of the ringing as well, regardless of the position where the voltage is detected along the winding. The proposed model also catches the different magnitudes of the voltage overshoots, which depend on their position along the winding.

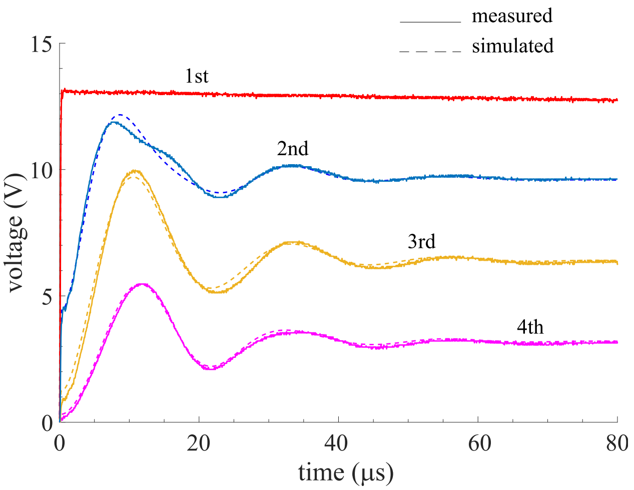

**Figure 14.** Comparison between the measured and the simulated response voltages at the interconnections between the pole windings, as represented in Figure 11. Input voltage applied at the winding directly: rising voltage edge 13 V, rise time 0.2 µs.

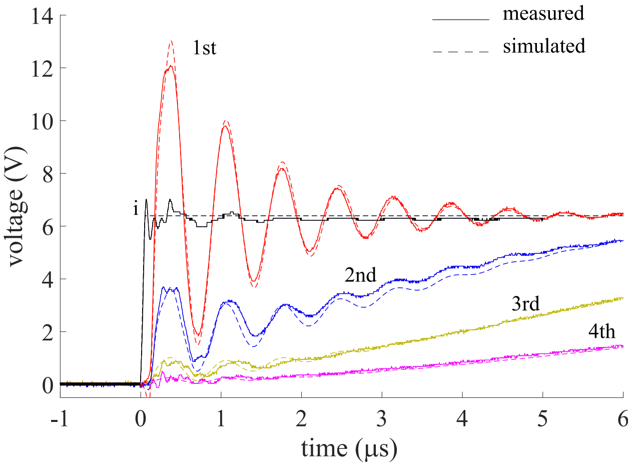

**Figure 15.** Comparison between the measured and the simulated response voltages at the interconnections between the pole windings, as represented in Figure 12. Input voltage applied through the feeder: rising voltage edge of 6.5 V with rise time 50 ns.

### 3.2. Second Experiment and Supercritical Transient Simulation

The second experiment considers a 6.5 V large voltage step with rise time 50 ns applied to the field winding terminals through the feeder. Figure 15 represents the comparison between the measured and simulated voltages at the interconnections between the pole windings.

The frequency of the voltage overshoots is roughly 1.4 Mhz, well beyond the critical frequency of the winding, which can be calculated by substituting (40) in (1)

$$f_c = \left(4\pi^2 \frac{k_w}{k}\right)^{-\frac{1}{2+\gamma_w}} = 95.8\,\mathrm{kHz}. \tag{43}$$

Since the voltage overshoot at the winding terminals is supercritical, it cannot propagate through the winding via the galvanic conduction. The mechanism for the reproduction of the overshoots at different winding sections is the electrostatic induction. This fact explains why there is no essential timely delay between the overshoots and why their amplitudes decay almost exponentially along the winding. In this way, the model proves to be able to describe the supercritical voltage distribution in the winding as well. As anticipated in the method, the attenuation in the cable due to the losses in the dielectric at high frequency cannot be easily estimated. In order to fit the simulated voltage overshoot to the measured one at the winding input terminals, a loss factor $\tan\delta_f = 0.02$ has been needed. With reference to the rubber insulated cable at high frequency, this value for $\tan\delta$ has the same order of magnitude as those given in the literature anticipated in the method.

If the interest of the overvoltage analysis is about to determine the voltage overshoot at the winding terminals only, the opportunity and convenience of developing a whole — even though simple — distributed parameter model for the field winding could be doubted. However, the following version of the second experiment sheds light on this point. In fact, Figure 16 shows the experimental effects of increasing the rise time of the voltage step applied to the field winding through the feeder. This time the feeder is supplied by the voltage edge generator shown in Figure 1.

In Figure 16, it can be observed that the not negligible internal impedance of the chosen supplying arrangement lets us observe voltage overshoots at the beginning of the feeder too. Thanks to multiple voltage wave reflections and interferences into the feeder, the relative overvoltage at the field winding terminal gets more than three times higher than the steady-state voltage (case of Figure 16(a)). Nevertheless, if the rise time increases, the amplitude of the overvoltage decreases. It can be noticed

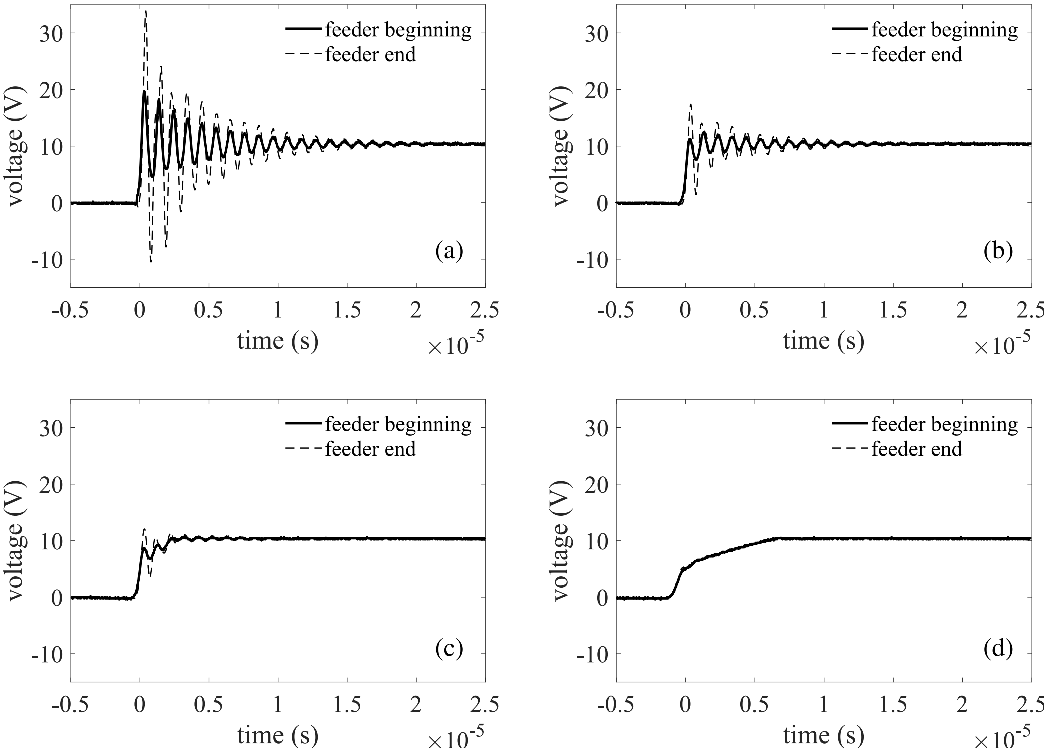

**Figure 16.** Voltage response at the beginning and at the end of the feeder for different rise times: (a) 0.29 µs, (b) 0.35 µs, (c) 1.50 µs, (d) 5.38 µs.

that, for a rise time slightly larger than 5 µs, the voltage overshoots disappear completely.

Considering the travelling wave theory developed by Rüdenberg [31], the portion $v(t)$ of the step voltage related to the harmonics which can penetrate the winding is

$$v\left(t\right)=\frac{V}{2}+\frac{V}{\pi}\int_0^{2\pi f_c}\frac{\sin\left(\omega t\right)}{\omega}\mathrm{d}\omega=\frac{V}{2}+\frac{V}{\pi}Si\left(2\pi f_c t\right), \tag{44}$$

where all the subcritical harmonics of the step voltage have been taken into account.

Setting

$$\zeta=f_c t, \tag{45}$$

Equation (44) becomes

$$\frac{v(\zeta)}{V}=\frac{1}{2}+\frac{1}{\pi}Si\left(2\pi\zeta\right), \tag{46}$$

that is represented in Figure 17.

Observing Figure 16 and considering (45), it can be recognized that in order to fully penetrate a winding showing a critical frequency $f_c$, the incident voltage step must present a maximal rise time $t_c$ equal to

$$t_c=\frac{1}{2f_c}. \tag{47}$$

Therefore, all voltage steps presenting a rise time $\tau < t_c$ must contain, beside $v(t)$, a residual voltage $\zeta\Delta v(\zeta)$, which is built up by all the supercritical harmonics, which cannot enter the winding. Such supercritical residual voltage is the trigger for the ringing, since it represents the first reflected voltage at the winding terminals essentially. Approximating the generic supercritical and critical voltage steps by the hyperbolic tangent functions, the normalized reflected voltage can be expressed by

$$\frac{\Delta v\left(\zeta,\chi\right)}{V}\cong\frac{1}{2}\tanh\left[\frac{4}{\chi}\left(\zeta-1+\chi\right)\right]-\frac{1}{2}\tanh\left(4\zeta\right), \tag{48}$$

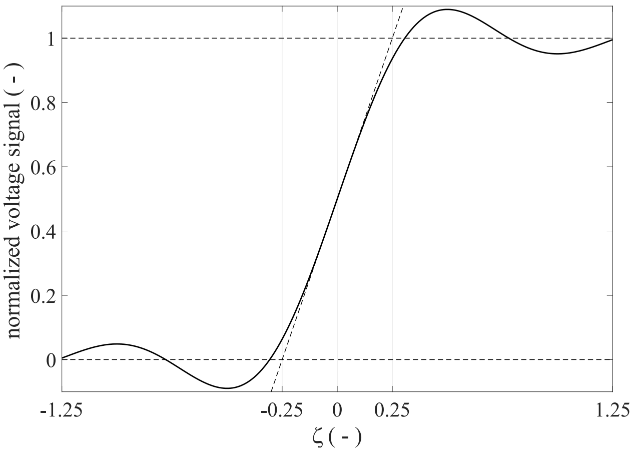

**Figure 17.** Normalized voltage signal which can penetrate the winding completely.

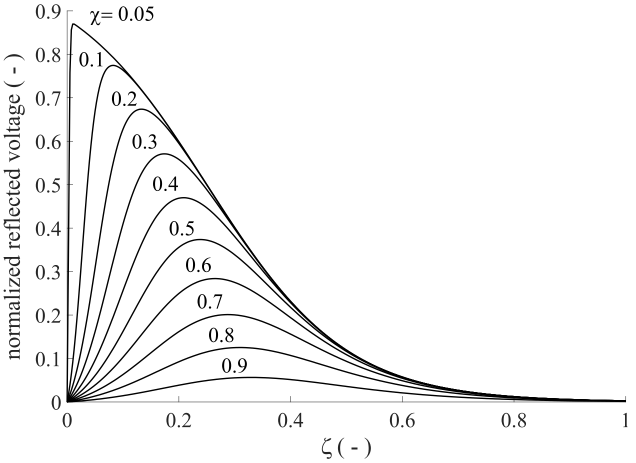

**Figure 18.** Intensity $\chi$ and relative position $\zeta$ of the voltage overshoot.

where

$$\chi = \frac{\tau}{t_c}. \tag{49}$$

Equation (48) is represented in Figure 18 for heuristic reasons only and shows that the shorter the rise time is, the larger the maximal value of the reflected voltage wave is.

At the limit, for $\chi = 1$, the input step voltage becomes the critical one of Figure 16, and no voltage wave reflection can take place at all.

Considering the actual winding critical frequency (43), the related critical rise time can be found by using (47)

$$t_c = \frac{1}{2f_c} \cong 5.22\,\mu\text{s}. \tag{50}$$

With reference to Figure 17, result (50) explains why the ringing is present only in those cases, where the rise time of the step voltage $\tau < 5.22\,\mu\text{s}$.

As soon as the voltage step becomes subcritical, the ringing disappears (see Figure 16(d)).

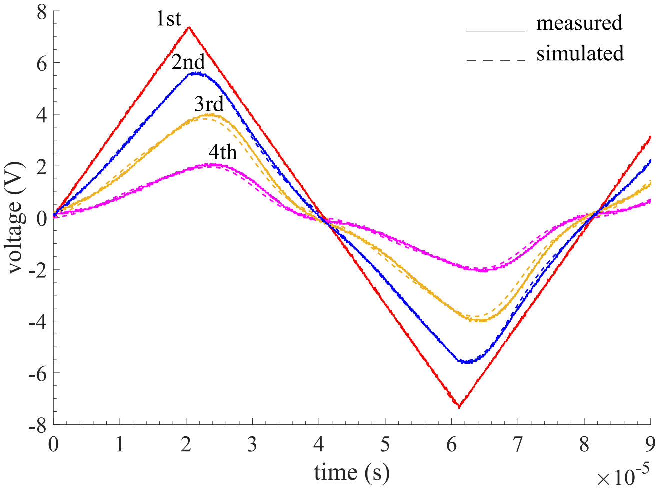

**Figure 19.** Comparison between the measured and the simulated response voltages at the interconnections between the pole windings, as represented in Figure 11. Input voltage applied to the winding directly: amplitude 7.5 V, frequency 12.3 kHz.

The considerations drawn till here show that a deep insight into the winding phenomena is needed, in order to perform the analysis of the overvoltages at the interface between feeder and field winding. This activity cannot be solely based on the feeder modelling, as it is the case, e.g., of the Bergeron's and Bewley's approach. The overvoltage analysis must rely on the interaction between the feeder model on one side and a winding model on the other.

### 3.3. Third Experiment and Periodic Steady-State Simulation

In the third and last experiment, the winding has been supplied at its terminals by a triangular wave generator having frequency 12.3 kHz and peak voltage 7.5 V, in order to check the response of the winding model for frequencies below the first natural one (42). Figure 19 shows the comparison between the simulated voltages and measured ones at the interconnections between the pole windings. The input signal has been approximated by the first six harmonics up to the 11th one.

These results prove that the winding model works fine in the periodic steady state as well, at relatively low frequency.

## 4. CONCLUSIONS

The presented model is able to reproduce voltage transients in highly inductive windings with frequency dependent parameters making use of the frequency analysis only. Based on a simplified transmission line model for both feeder and load, it has been proven to require a minimal set of parameters for reproducing accurately fast voltage transients and periodic steady-state behaviour. The novelty of the model is that contrary to the Bergeron's or Bewely's method, it can handle non-TEM propagation typical of electrical machines windings, and it allows an insight into the transient phenomena in the feeder and/or in the winding, not only at their beginning and end. Moreover, it needs neither numerical integration of differential equations nor the calculation of convolution integrals in order to provide a solution in the time domain. The suggested model accurately simulates the sub- as well as the supercritical behaviour of the winding. The most important phenomena regarding the propagations of voltage surges in the feeder-winding coupling are well reproduced, where the simplicity of the transmission line model makes it evident which parameters influence the overshoot frequency and which ones influence their damping. Although more complicated winding arrangements could require some changes and specific adaptations in the suggested model, the conclusions drawn about the role and relevance of the winding parameters will keep their general validity. The model is particularly useful for studying voltage transient in all those windings where the current gets regulated by means of switching power electronics, especially when the rapidity of the voltage rising/falling edge is such to trigger propagation phenomena.

## ACKNOWLEDGMENT

This project has received funding from the European Union's Horizon 2020 research and innovation programme under grant agreement No. 764011.

## DATA AVAILABILITY STATEMENT

The data that support the findings of this study are available from the corresponding author, R.F., upon reasonable request.

## APPENDIX A.

The eddy current losses per unit length $W_s$ ($\mathrm{Wm}^{-1}$) produced in a cylindrical massive copper conductor of diameter $D_s$ by an uniform transversal harmonic magnetic field $H$ with angular frequency $\omega$ can be expressed according to [35] as

$$W_{s,fp} = \frac{D_s^2}{512\pi^2} \frac{\omega^2 \mu_0^2}{R_0} H^2 \tag{A1}$$

when the conductor is fully penetrated and by

$$W_{s,pp} = \frac{D_s^2}{16}\sqrt{\frac{R_0\mu_0\omega}{8\pi}}H^2 \tag{A2}$$

when it is not fully penetrated.

The parameter $R_0$ represents the DC-resistance of the conductor which can be expressed as

$$R_0 = \frac{4\mu_0\omega}{\pi}\left(\frac{\delta}{D_s}\right)^2. \tag{A3}$$

By substituting (A3) in (A1), the following expression for the specific losses can be obtained, when the conductor is fully penetrated

$$W_{s,fp} = \frac{\rho}{2048\pi}\left(\frac{D_s}{\delta}\right)^4 H^2. \tag{A4}$$

By substituting (A3) in (A2), the following expression for the specific losses can be obtained when the conductor is not fully penetrated

$$W_{s,pp} = \frac{\rho}{16\sqrt{2}\pi}\frac{D_s}{\delta}H^2 \tag{A5}$$

In a bundle of $n_s$ twisted or transposed strands with overall diameter $D_w$, it is possible to consider the current equal in all strands. The reason for this is that along the unit length of the wire all strand positions are in average equally possible for each strand, due to strand transposition. The twisting also produces a similar effect even though it is not as effective as the transposition.

Approximating the stranded wire as a solid one and crossed by a uniform current density $J$, it is possible to find an average value for the magnetic field $H^2_{AVG}$ in the bundle cross section by

$$H^2_{AVG} = \frac{4}{\pi D_w^2}\int_0^{D_{w/2}}\left(\frac{rJ}{2}\right)^2 2\pi r dr = \frac{1}{2\pi^2}\left(\frac{I}{D_w}\right)^2 \tag{A6}$$

The losses due to the internal proximity effect in the conductor, when the strand is fully penetrated, are then,

$$W_{s,fp} = \frac{\rho}{4096\pi}\left(\frac{D_s}{\delta}\right)^4\left(\frac{I}{D_w}\right)^2. \tag{A7}$$

From (A7), the contribution to the AC-resistance of the wire due to the proximity effect can be expressed as

$$\Delta R_{w,fp} = \frac{\rho}{2048\pi^3}\left(\frac{D_s}{\delta}\right)^4\frac{n_s}{D_w^2}. \tag{A8}$$

Since the DC-resistance of the wire is

$$R_{w,DC} = \frac{R_0}{n_s} = \frac{4\mu_0\omega}{n_s\pi}\left(\frac{\delta}{D_s}\right)^2, \tag{A9}$$

the $\Delta R_{w,fp}$ can be expressed as

$$\Delta R_{w,fp} = R_{w,DC}\frac{1}{8192\pi^2}\left(\frac{D_s}{\delta}\right)^4\left(\frac{n_s D_s}{D_w}\right)^2. \tag{A10}$$

The losses due to the internal proximity effect in the conductor when the strand is not fully penetrated can be obtained combining (A2) and (A6)

$$W_{w,pp} = n_s W_s = n_s\frac{\rho}{32\sqrt{2}\pi^3}\frac{D_s}{\delta}\left(\frac{I}{D_w}\right)^2 \tag{A11}$$

The contribution to the AC-resistance of the wire due to the internal proximity effect when the strand is partially penetrated is then

$$\Delta R_{w,pp} = \frac{\rho}{16\sqrt{2}\pi^3}\frac{D_s}{\delta}\frac{n_s}{D_w^2}. \tag{A12}$$

Considering the DC-resistance of the wire given in (A3), $\Delta R_{w,pp}$ can be expressed as

$$\Delta R_{w,pp} = R_{w,DC} F_{prox}. \tag{A13}$$

where

$$F_{prox} = \frac{1}{64\sqrt{2}\pi^2}\frac{D_s}{\delta}\left(\frac{n_s D_s}{D_w}\right)^2. \tag{A14}$$

The frequency for which $\Delta R_{w,pp} = \Delta R_{w,fp}$ is

$$f_{dis} = \frac{8\sqrt[3]{2}}{\pi}\frac{\rho}{\mu_0 D_s^2} \tag{A15}$$

The AC resistance due to the skin effect in the strand can be taken into account using the approximation given by [36] for the fully and partially penetrated strands, respectively. For a fully penetrated strand

$$R_{w,skin\_fp} = R_{w,DC}\left[1 + \frac{1}{768}\left(\frac{D_s}{\delta}\right)^4\right]. \tag{A16}$$

and for the partially penetrated strand

$$R_{w,skin\_pp} = R_{w,DC} F_{skin}, \tag{A17}$$

where

$$F_{skin} = \frac{D_s}{4\delta} + \frac{1}{4} + \frac{3}{16}\frac{\delta}{D_s}. \tag{A18}$$

Equation (A16) approximates the real value of the AC-resistance in defect for less than −3% when $D_s/\delta < 3.25$, which means for a frequency

$$f < f_{skin\_fp} = \frac{13}{2\pi}\frac{\rho}{\mu_0 D_s^2}. \tag{A19}$$

Equation (A17) approximates the real value of the AC-resistance in defect for less than −3% when $D_s/\delta > 4$, which means for

$$f > f_{skin\_pp} = \frac{8}{\pi}\frac{\rho}{\mu_0 D_s^2}. \tag{A20}$$

## REFERENCES

1. Martinez, J. A., D. Goldsworthy, and R. Horton, "Switching overvoltage measurements and simulations — Part I: Field test overvoltage measurements," *IEEE Trans. Power Deliv.*, Vol. 29, No. 6, 2502–2509, 2014, doi: 10.1109/TPWRD.2014.2303575.
2. Popov, M., L. van der Sluis, and G. C. Paap, "Investigation of the circuit breaker reignition overvoltages caused by no-load transformer switching surges," *Euro. Trans. Electr. Power*, Vol. 11, 413–422, 2007, doi: 10.1002/etep.4450110609.
3. Zheng, Y., C. Li, M. Wu, Z. Wei, C. Gong, and X. Sun, "Influence of circuit breaker features on switching overvoltage of 35 kV shunt reactor on no-load busbar — II. On site testing and comparison," *8th Renewable Power Generation Conference (RPG 2019)*, 1–4, Shanghai, China, 2019, doi: 10.1049/cp.2019.0265.
4. Wouters, P., A. van Deursen, and M. Vermeer, "Methodology and accuracy for non-invasive detection of switching transient overvoltages from compensation coils connected to power transformers," *IET Sci. Meas. Technol.*, Vol. 14, No. 2, 173–181, 2020, doi: 10.1049/iet-smt.2019.0228.
5. Benešová, Z., V. Kotlan, and R. Haller, "Influence of transmission line wave properties on surge voltage wave propagation," *18th International Conference on Computational Problems of Electrical Engineering (CPEE)*, 1–4, Kutna Hora, 2017, doi: 10.1109/CPEE.2017.8093064.

6. Furgał, J., M. Kuniewski, and P. Pajak, "Analysis of internal overvoltages in transformer windings during transients in electrical networks," *Energies*, Vol. 13, No. 2644, 1–20, 2020, doi: 10.3390/en13102644.
7. "IEEE standard for insulation coordination — Definitions, principles, and rules," *IEEE Std 1313.1-1996*, 1996, doi: 10.1109/IEEESTD.1996.81077.
8. Biela, J., M. Schweizer, S. Waffler, and J. W. Kolar, "SiC versus Si-evaluation of potentials for performance improvement of inverter and DC-DC converter systems by SiC power semiconductors," *IEEE Trans. Ind. Electron.*, Vol. 58, No. 7, 2872–2882, 2011, doi: 10.1109/TIE.2010.2072896.
9. Ranstad, P., H. Nee, J. Linnér, and D. Peftitsis, "An experimental evaluation of SiC switches in soft-switching converters," *IEEE Trans. Power Electr.*, Vol. 29, No. 5, 2527–2538, 2014, doi: 10.1109/TPEL.2013.2265380.
10. Ruffo, R., P. Guglielmi, and E. Armando, "Inverter side RL filter precise design for motor overvoltage mitigation in SiC-based drives," *IEEE Trans. Ind. Electron.*, Vol. 67, No. 2, 863–873, 2020, doi: 10.1109/TIE.2019.2898623.
11. Hameyer, K., A. Ruf, and F. Pauli, "Influence of fast switching semiconductors on the winding insulation system of electrical machines," *International Power Electronics Conference (IPEC-Niigata 2018-ECCE Asia)*, 740–745, Niigata, 2018, doi: 10.23919/IPEC.2018.8507972.
12. Tran, D., G. Segond, and V. Dossantos, "Modeling and analysis of EMI and overvoltage phenomenon in sic inverter driven motor at high switching frequency," *2018 IEEE 18th International Power Electronics and Motion Control Conference (PEMC)*, 268–273, Budapest, 2018, doi: 10.1109/EPEPEMC.2018.8521882.
13. Zoeller, C., M. A. Vogelsberger, T. M. Wolbank, and H. Ertl, "Impact of SiC semiconductors switching transition speed on insulation health state monitoring of traction machines," *IET Power Electron.*, Vol. 9, No. 15, 2769–2775, 2016, doi: 10.1049/iet-pel.2015.0988.
14. Wang, P., H. Xu, J. Wang, W. Zhou, and A. Cavallini, "The influence of repetitive square wave voltage rise time on partial discharge inception voltage," *2016 IEEE Conference on Electrical Insulation and Dielectric Phenomena (CEIDP)*, 759–762, Toronto, 2016, doi: 10.1109/CEIDP.2016.7785635.
15. Benmamas, L., P. Teste, E. Odic, G. Krebs, and T. Hamiti, "Contribution to the analysis of PWM inverter parameters influence on the partial discharge inception voltage," *IEEE Trans. Dielectr Electr. Insul.*, Vol. 26, No. 1, 146–152, 2019, doi: 10.1109/TDEI.2018.007787.
16. Amarir, S. and K. Al-Haddad, "Overvoltages computation algorithm for motors fed from long cable PWM drives," *MELECON 2008 — The 14th IEEE Mediterranean Electrotechnical Conference*, 554–559, Ajaccio, 2008, doi: 10.1109/MELCON.2008.4618493.
17. Bergeron, L. J. B., "Du coup de bêlier en hydraulique au coup de foudre en électricité," 336, Dunod, Paris 1950.
18. Pulsinelli, F., L. Solero, D. Chiola, K. Sobe, and F. Brucchi, "Overvoltages at motor terminals in SiC electric drives," *2018 International Symposium on Power Electronics, Electrical Drives, Automation and Motion (SPEEDAM)*, 513–518, Amalfi, 2018, doi: 10.1109/SPEEDAM.2018.8445203.
19. Bewley, L. V., "Traveling waves on transmission systems," *Trans. AIEE*, Vol. 50, No. 2, 532–550, 1921, doi:10.1109/T-AIEE.1931.5055827.
20. Sajid, M., M. Surykalavathi, and B. P. Singh, "Measurement and calculation of voltage stress in industrial motor due to fast surges," *INAE, Lett.*, Vol. 4, 83–90, 2019, doi: 10.1007/s41403-019-00068-8.
21. Kotlan, V. and Z. Benešová, "Overvoltage propagation from transmission line into transformer winding," *Adv. Electr. Electron. Eng.*, Vol. 13, No. 5, 2015, 478–483, doi: 10.15598/aeee.v13i5.1421.
22. Felicetti, R., C. J. D. Abrahamsson, and U. Lundin, "Experimentally validated model of a fast switched salient pole rotor winding," *2019 IEEE Workshop on Electrical Machines Design, Control and Diagnosis (WEMDCD)*, 150–156, Athens, Greece, 2019, doi: 10.1109/WEMDCD.2019.8887777.

23. Caniggia, S. and F. R. Maradei, *Signal Integrity and Radiated Emission of High-Speed Digital Systems*, 482, John Wiley & Sons Ltd., New York, 2008.
24. *Transient Analysis of Power Systems: Solution Techniques, Tools and Applications*, J. A. Martinez-Velasco, J. A Martinez-Velasco, ed., 72–99, John Wiley & Sons, Incorporated, ProQuest Ebook Central, 2015, https://ebookcentral.proquest.com/lib/uu/detail.action?docID=1875897.
25. Smajic, J., M. Bucher, T. Franz, B. Crangranu-Cretu, A. Shoory, and J. Tepper, "Modeling of frequency dependent parameters in time domain high frequency transformer simulations," *Procedia Engineering*, Vol. 202, 251–263, 2017, doi: 10.1016/j.proeng.2017.09.712.
26. Theocharis, A. and M. Popov, "A piece-wise linearized transformer winding model for the analysis of internal voltage propagation," *2019 IEEE Milan PowerTech*, 1–6, Milan, 2019, doi: 10.1109/PTC.2019.8810920.
27. Morched, A., L. Marti, and J. Ottevangers, "A high frequency transformer model for the EMTP," *IEEE Trans. Power Deliv.*, Vol. 8, No. 3, 1615–1626, 1993, doi: 10.1109/61.252688.
28. *Transient Analysis of Power Systems: Solution Techniques, Tools and Applications*, J. A. Martinez-Velasco and J. A Martinez-Velasco (eds.), 57–60, John Wiley & Sons, Incorporated, ProQuest Ebook Central, 2015, https://ebookcentral.proquest.com/lib/uu/detail.action?docID=1875897.
29. Manyahi, M. J., M. Leijon, and R. Thottappillil, "Transient response of transformer with XLPE insulation cable winding design," *Int. J. Electr. Power Energy Syst.*, Vol. 27, No. 1, 69–80, 2005, doi: 10.1016/j.ijepes.2004.07.010.
30. Nøland, J. K., S. Nuzzo, A. Tessarolo, et al., "Excitation system technologies for wound-field synchronous machines: Survey of solutions and evolving trends," *IEEE Access*, Vol. 7, 109699–109718, 2019.
31. Rüdenberg, R., "Performance of travelling waves in coils and windings," *AIEE Transactions*, Vol. 59, 1031–1045, 1940.
32. Heller, B. and A. Veverka, *Surge Phenomena in Electrical Machines*, 29, Publishing House of the Czechoslovak Academy of Sciences, Prague, 1968.
33. Kim, C., Z. Jin, P. Jiang, Z. Zhu, and G. Wang, "Investigation of dielectric behavior of thermally aged XLPE cable in the high-frequency range," *Polymer Testing*, Vol. 25, No. 4, 553–561, 2006, doi: 10.1016/j.polymertesting.2006.03.009.
34. Felicetti, R., C. D. J. Abrahamsson, and U. Lundin, "An experimentally determined field winding model with frequency dependent parameters," *IET Electr. Power Appl.*, Vol. 15, No. 6, 696–716, 2021, doi: 10.1049/elp2.12061.
35. Butterworth, S., "Eddy-current losses in cylindrical conductors, with special applications to the alternating current resistances of short coils," *Philosophical Transactions of the Royal Society of London*, Series A, Vol. 222, 57–100, 1922.
36. Stoll, R. L., *Analysis of Eddy Currents*, 25, Clarendon Press, Oxford, 1974.